

# Exploring the thermal energy contents of the intergalactic medium with the Sunyaev-Zel’dovich effect

S.H. Lim<sup>1\*</sup>, H.J. Mo<sup>1,2</sup>, Huiyuan Wang<sup>3</sup>, Xiaohu Yang<sup>4</sup>

<sup>1</sup>*Department of Astronomy, University of Massachusetts, Amherst MA 01003-9305, USA*

<sup>2</sup>*Physics Department and Center for Astrophysics, Tsinghua University, Beijing 10084, China*

<sup>3</sup>*Key Laboratory for Research in Galaxies and Cosmology, Department of Astronomy, University of Science and Technology of China, Hefei, Anhui 230026, China; School of Astronomy and Space Science, University of Science and Technology of China, Hefei 230026, China*

<sup>4</sup>*Department of Astronomy, Shanghai Key Laboratory for Particle Physics and Cosmology, Shanghai Jiao Tong University, Shanghai 200240, China; IFSA Collaborative Innovation Center, and Tsung-Dao Lee Institute, Shanghai Jiao Tong University, Shanghai 200240, China*

Accepted ..... Received .....; in original form .....

## ABSTRACT

We examine the thermal energy contents of the intergalactic medium (IGM) over three orders of magnitude in both mass density and gas temperature using thermal Sunyaev-Zel’dovich effect (tSZE). The analysis is based on *Planck* tSZE map and the cosmic density field, reconstructed for the SDSS DR7 volume and sampled on a grid of cubic cells of  $(1h^{-1}\text{Mpc})^3$ , together with a matched filter technique employed to maximize the signal-to-noise. Our results show that the pressure - density relation of the IGM is roughly a power law given by an adiabatic equation of state, with an indication of steepening at densities higher than about 10 times the mean density of the universe. The implied average gas temperature is  $\sim 10^4$  K in regions of mean density,  $\rho_m \sim \bar{\rho}_m$ , increasing to about  $10^5$  K for  $\rho_m \sim 10\bar{\rho}_m$ , and to  $> 10^6$  K for  $\rho_m \sim 100\bar{\rho}_m$ . At a given density, the thermal energy content of the IGM is also found to be higher in regions of stronger tidal fields, likely due to shock heating by the formation of large scale structure and/or feedback from galaxies and AGNs. A comparison of the results with hydrodynamic simulations suggests that the current data can already provide interesting constraints on galaxy formation.

**Key words:** methods: statistical – galaxies: formation – galaxies: evolution – galaxies: haloes.

## 1 INTRODUCTION

The baryon mass that has been identified by current observations in galaxies and galaxy systems in the  $z \sim 0$  universe accounts for about 2% of the critical density (e.g. Fukugita et al. 1998; Fukugita & Peebles 2004), which is about one third of the cosmic baryon abundance predicted by the primordial nucleosynthesis (e.g. Olive et al. 2000) and required to explain the fluctuations in the cosmic microwave background radiation (CMB) (e.g. Hinshaw et al. 2013; Planck Collaboration XIII 2016). Thus, a large fraction of baryons must be contained in the intergalactic medium. Indeed, observations of the Ly $\alpha$  forest at low- $z$  suggest that about 30 – 40% of the cosmic baryons may be hidden in the forest (e.g. Danforth & Shull 2008), but the results are still very

uncertain, because the sample of low- $z$  forest is small and because of uncertainties in the ionization correction that is needed to obtain the total hydrogen density.

Cosmological simulations have shown that the cosmic baryons in the low- $z$  universe can exist in a variety of forms. In addition to stars and cold gas that are associated with galaxies, some baryons are predicted to be contained in the hot gaseous halos that are produced by the collapse of dark matter halos and feedback of galaxy formation. Furthermore, many gas simulations demonstrated that a large fraction of the baryons in the low- $z$  universe actually reside in a diffuse warm-hot intergalactic medium (WHIM) (e.g. Cen & Ostriker 1999; Davé et al. 1999, 2001), with temperature in the range between  $10^5$  and  $10^7$  K. This medium is generated by a combination of feedback from galaxy formation and shocks accompanying the formation of the large-scale

\* E-mail: slim@astro.umass.edu

structure (e.g. Sunyaev & Zeldovich 1972; Nath & Silk 2001; Furlanetto & Loeb 2004; Rasera & Teysier 2006).

Clearly, a comprehensive investigation of all gas components is required to have a complete understanding of how galaxies and larger scale structure form and evolve in the universe. In particular, the study of the WHIM, which is potentially the dominating gas component in the low- $z$  universe but yet poorly understood so far, is important not only for obtaining a complete census of the cosmic baryons, but also for understanding how galaxies and structure formation interact with the gas component in the universe. Indeed, observations of Ly $\alpha$  absorption systems have revealed that the intergalactic medium (IGM) at  $z \sim 0$  is significantly enriched in metal, indicating that a significant fraction of baryons may have been ejected from galaxies and moved to the IGM by dynamical processes, such as winds driven by stellar and AGN feedback or by ram-pressure stripping (e.g. Aguirre et al. 2001). In addition, the similarity in the metallicities of the intra-cluster media (ICM) observed for different clusters suggests that the formation of the ICM is perhaps dominated by inflow of the gas from the large scale cosmic web (e.g. Werner et al. 2013; Ettori et al. 2015; McDonald et al. 2016; Mantz et al. 2017). Both of these demonstrate the importance of the interaction between galaxies and gas in shaping the gas media we observe. However, the detection of the WHIM in observations is challenging. At a temperature of  $T \sim 10^5$ - $10^7$  K, the gas is almost completely ionized, making it difficult to detect in absorption. The low density of the WHIM also makes it difficult to detect in UV and X-ray emission.

With the advent of large surveys of the cosmic microwave background (CMB), a promising new avenue is opened up. As the CMB photons travel to reach us, they are scattered by free electrons associated with hot gas via Compton scattering. This produces a change in the energy distribution of the CMB photons, an effect referred to as the thermal Sunyaev-Zel'dovich effect (tSZE; Sunyaev & Zeldovich 1972). The tSZE is a measure of the projected electron pressure along the line of sight, and so it provides a way to probe the thermal energy content of the ionized gas in the universe. Compared to X-ray emissions, the tSZE is more sensitive to diffuse gas, making it more suitable for probing relatively low-density media, such as WHIM. It also complements absorption studies of highly ionized gas, as ionization correction and gas metallicity are not needed to obtain the total gas content.

Great amounts of effort have been made to measure the tSZE from observational data. Planck Collaboration XI (2013) used the *Planck* multi-frequency CMB temperature maps and a sample of locally brightest galaxies to study the tSZE produced by galaxy systems down to a halo mass  $\sim 4 \times 10^{12} M_{\odot}$ . Remarkably, they found that their results are consistent with the self-similar model in which the hot gas fraction in halos is independent of halo mass. A similar conclusion was also reached by Greco et al. (2015) using a similar method. Tanimura et al. (2017) and de Graaff et al. (2017) reported the detection of warm-hot gas in cosmic filaments by cross-correlating filaments identified by galaxy pairs with the *Planck* tSZE map. By cross correlating the *Planck* tSZE map with the mass density map obtained from the gravitational lensing data of the CFHTLenS survey, Van Waerbeke et al. (2014); Ma et al. (2015); Hojjati et al. (2015)

found significant correlations between the gas and dark matter distributions. Finally, Hill & Spergel (2014) reported a significant detection of cross-correlation between the *Planck* CMB lensing potential map and the *Planck* tSZE map. All these indicate that tSZE provides a powerful way to investigate the gas distribution in the universe.

Recently, Lim et al. (2018a,b) used the group catalogs of Yang et al. (2007) and Lim et al. (2017) to extract, from the *Planck* CMB observation, both the tSZE and kinematic SZ effects (kSZE) of the warm-hot gas associated with halos of different masses. They employed the matched filter technique (Haehnelt & Tegmark 1996; Herranz et al. 2002; Melin et al. 2005, 2006) to maximize the signal-to-noise ratio. In particular, they matched the filter simultaneously to all galaxy groups to constrain the corresponding signals jointly as a function of group mass, so as to minimize projection effects for groups lying closely in the sky. Combining the tSZE and kSZE, they found that the total amount of the baryons associated with dark matter halos are consistent with the universal baryon fraction, even in low-mass halos, but that the gas temperature is much lower than the virial temperature in low-mass halos. Various tests performed demonstrate that the method is very powerful in extracting the SZE signals effectively and reliably.

In this paper, we study the thermal contents of the IGM at  $z \sim 0$ , extending the analyses of Lim et al. (2018a,b) by going beyond scales of dark matter halos. Specifically, we constrain the pressure of the gas in different environments, using the total density field reconstructed by Wang et al. (2009, 2016) in the Sloan Digital Sky Survey Data Release 7 (SDSS DR7) volume and using the *Planck* tSZE map as the observational constraint. As we will see, our analysis is able to provide constraints on the thermal energy contents of the WHIM in regions covering almost three orders of magnitude in mass density. In particular, our results are shown to be capable of providing constraints on models of galaxy formation. The outline of this paper is as follows. We describe the data used in our analysis in Section 2, and our method to constrain the gas pressure in Section 3. We present our main results and comparisons with results from numerical simulations in Section 4. We summarize and conclude in Section 5.

## 2 DATA

### 2.1 The *Planck* $y$ -map

The temperature change in the CMB spectrum by the tSZE is given by

$$\left( \frac{\Delta T}{T_{\text{CMB}}} \right) = g(x)y \equiv g(x) \frac{\sigma_{\text{T}}}{m_e c^2} \int P_e dl, \quad (1)$$

where  $y$  is the Compton parameter,  $g(x) = x \coth(x/2) - 4$  is the conversion factor at a given  $x \equiv h\nu/(k_{\text{B}}T_{\text{CMB}})$ ,  $T_{\text{CMB}} = 2.7255$  K,  $\sigma_{\text{T}}$  is the Thompson cross-section,  $m_e$  is the electron rest-mass,  $c$  is the speed of light,  $P_e = n_e k_{\text{B}} T_e$  is the electron pressure with  $n_e$  the free electron density, and  $dl$  is the path length along each line-of-sight (LOS). The *Planck* (Tauber et al. 2010; Planck Collaboration I 2011) is an all-sky observation of the CMB in nine frequency bands from 30 to 857 GHz, with angular resolutions ranging between  $5'$  and  $31'$ . We use the *Planck* MILCA (Modified Internal Linear Combination Algorithm; Hurier et al. 2013) all-sky

tSZ Compton parameter map (Planck Collaboration XXII 2016), also known as the MILCA  $y$ -map, which is part of the *Planck* 2015 data release †. The MILCA  $y$ -map is constructed from the full mission data set of the *Planck*, using a combination of different frequency maps to minimize the primary CMB fluctuations and the contamination from foreground sources. The details about the  $y$ -map construction can be found in the original papers. We mask the brightest 40% of the sky to limit the Galactic foreground contamination, by using the corresponding mask provided in the *Planck* 2015 data release. We also apply the mask for point sources, provided in the same data release, to reduce the contamination from radio and infrared sources.

As a test, we have also applied the same analysis to the NILC (Needlet Independent Linear Combination; Remazeilles et al. 2011)  $y$ -map (Planck Collaboration XXII 2016), which treats dust contamination differently than the MILCA. No significant change is found in our results.

## 2.2 The dark matter density field in the SDSS DR7 volume

Another set of data that we use for our analysis is the reconstructed cosmic density field in Sloan Digital Sky Survey Data Release 7 (SDSS DR7; Abazajian et al. 2009) volume given by Wang et al. (2016) (W16). The reconstruction uses galaxy groups selected with the halo-based group finder (Yang et al. 2005, 2007) to represent dark matter halos. Extensive tests using mock galaxy redshift surveys constructed from the conditional luminosity function (CLF) model (e.g. Yang et al. 2003; van den Bosch et al. 2003) and semi-analytical models (Kang et al. 2005) revealed that this group finder is very successful in grouping galaxies into their common dark matter halos (see Yang et al. 2007). By partitioning the SDSS volume into domains associated with individual groups, and by modelling the mass distribution in each domain using profiles calibrated with  $N$ -body simulations, W16 reconstructed the real space density field within the entire SDSS DR7 volume. W16 used groups of halo masses  $M_h \geq 10^{12} h^{-1} M_\odot$ , so that completeness can be achieved to  $z \sim 0.12$ . The reconstruction was restricted to the contiguous region of the SDSS DR7 in the Northern Galactic Cap of  $\sim 7,000 \text{ deg}^2$ . While W16 provides the density field smoothed on various scales, we use the density field smoothed on  $1 h^{-1} \text{ Mpc}$  for our analysis.

## 2.3 Hydrodynamic simulations for comparison

To compare with our results, we use two recent cosmological hydrodynamic simulations. The first is Illustris (Nelson et al. 2015), which follows the evolution of the simulated Universe in a box of  $(106.5 \text{ Mpc})^3$ , implementing physical processes such as radiative cooling, star formation, and various feedback processes. The free parameters in sub-grid models were constrained by observations as well as simulations of higher resolutions. We use Illustris-1, their flagship run, which has the highest mass resolution, with gas particle mass

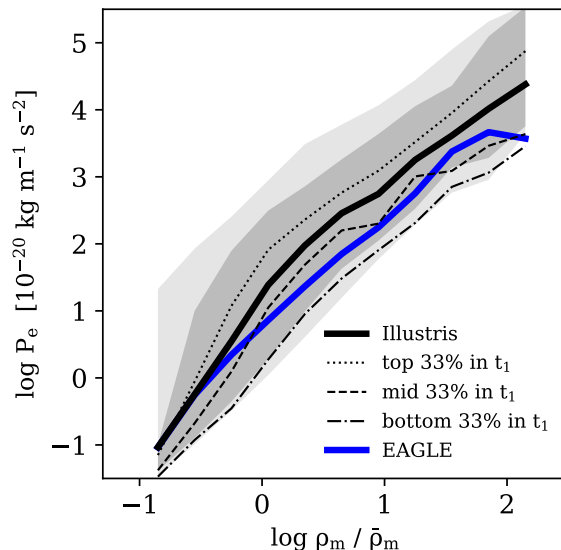


**Figure 1.** The relations between the electron pressure and mass density for grid-cells of  $1 (h^{-1} \text{ Mpc})^3$  obtained from Illustris and EAGLE. The solid lines show the mean relations, and the gray bands show the  $1\sigma$  and  $2\sigma$  dispersion obtained from Illustris. The thin lines show the mean relations obtained for the three sub-samples of the grid-cells according to the ranking in the tidal field strength,  $t_1$ , at given density, obtained from Illustris.

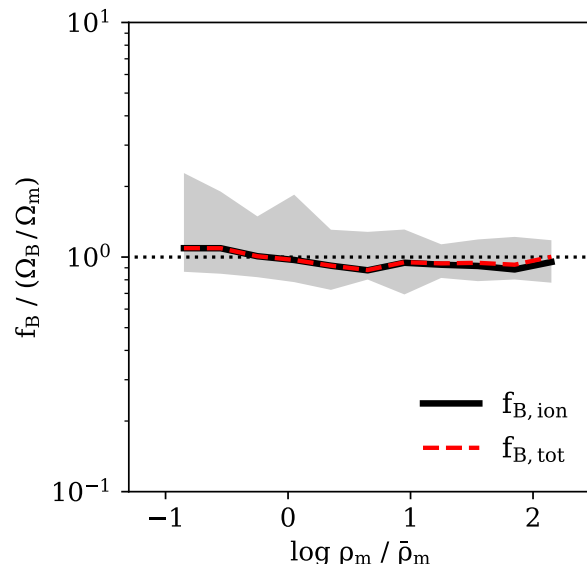


**Figure 2.** The ionized gas mass fraction, normalized by the cosmic mean baryon fraction, in grid-cells as a function of mass density as obtained from Illustris. The thick line shows the mean relation, while the shaded region indicates the  $1\sigma$  dispersion. For comparison the dashed line shows the average total baryon fraction as a function of mass density.

† <https://pla.esac.esa.int>

of  $1.6 \times 10^6 M_\odot$ . The simulation adopted WMAP9 cosmology, with  $\Omega_m = 0.273$ ,  $\Omega_\Lambda = 0.727$ ,  $h = 0.704$ , and a baryon fraction,  $\Omega_B/\Omega_m = 0.165$  (Hinshaw et al. 2013).

Another simulation we use is the Evolution and Assembly of GaLaxies and their Environments (EAGLE; Schaye et al. 2015; Crain et al. 2015; McAlpine et al. 2015). EAGLE implemented sub-grid physics models for cooling, star formation, and stellar and AGN feedback to evolve different types of particles, such as gas, stars, dark matter, and black holes. The parameters for these models are tuned to match a set of observations, such as the stellar mass function and stellar mass - black hole mass relation at  $z \sim 0$ . EAGLE provides a number of simulations assuming different model parameters and box sizes. We present results based on the ‘RefL0100N1504’ run, their fiducial simulation, which has the largest box size,  $(100 \text{ Mpc})^3$ , among all the EAGLE runs. Our tests showed that the results used for our comparisons were not significantly affected if other simulations were used. EAGLE assumes the *Planck* cosmology,  $(\Omega_m, \Omega_\Lambda, h) = (0.307, 0.693, 0.678)$  (Planck Collaboration XIII 2016).

Fig. 1 shows the pressure - density relation averaged over grid-cells of  $1 (h^{-1} \text{ Mpc})^3$  in the simulations. The cell size chosen here is to match the size adopted in our analysis. The mean relations, presented by the thick solid lines, have slopes roughly consistent with the adiabatic equation of state,  $P_e \sim \rho^{5/3}$  for both simulations. However, the average pressure at  $\rho_m > \bar{\rho}_m$  predicted by Illustris is about two to three times as high as that predicted by EAGLE, presumably because of cosmic variance and of the differences in the feedback models adopted in the two simulations. The scatter in pressure at a given density (the gray bands showing the  $1\sigma$  and  $2\sigma$  dispersion given by Illustris) is also very large. This large scatter motivates us to explore the possibility of a second parameter, in addition to density, that can affect the gas pressure (see §2.4).

On the scale of a grid cell, the distribution of baryons is expected to approximately follow that of the dark matter. Since most of the baryons are expected to be in the state of diffuse ionized gas, the total amount of ionized gas in a grid cell is roughly that given by the universal baryon fraction. Fig. 2 shows that this is indeed the case, at least in simulations. This result will be used to interpret the tSZE obtained from the observational data.

## 2.4 The large-scale tidal field

We have tested a number of quantities available from the simulation to see how they affect the gas pressure. These include stellar mass, star formation rate, black hole mass, mean velocity, velocity dispersion, the fluctuation in dark matter density, distance to nearest halos, fraction of mass contained in halos, and local tidal field, all estimated for individual grid cells that are used to sample the density field. We found that, among these quantities, the large-scale tidal field is the most significant second parameter that can change the gas pressure on top of the dependence on local dark matter density.

In our analysis, we tested two definitions of large-scale tidal field, one based on dark matter halos and the other based on the mass density field. We find that both definitions of the tidal field give practically the same results in our analysis [see Wang et al. (2011) for details of how the two

tidal fields are correlated]. In what follows, we only present results using the halo-based tidal field. The estimate of the halo-based tidal field is based on the halo tidal force along a direction  $\mathbf{t}$  exerted on the surface of a sphere of diameter  $1 h^{-1} \text{ Mpc}$  that approximates a grid-cell, normalized by the self-gravity of the matter inside the grid-cell,

$$f(\mathbf{t}) = \frac{\sum_i GM_i R_g (1 + 3 \cos 2\theta_i) / r_i^3}{2GM_g / R_g^2} \quad (2)$$

where the summation is over all the halos,  $M_i$  is the mass of halo  $i$ ,  $R_g = 0.5 h^{-1} \text{ Mpc}$  is the radius of the sphere that approximates the grid-cell,  $M_g$  is the mass enclosed within the grid-cell in question,  $r_i$  is the separation between the center of the grid-cell and the  $i$ -th halo, and  $\theta_i$  is the angle between  $\mathbf{t}$  and  $\mathbf{r}_i$  (e.g. Wang et al. 2011). So defined, the tidal field measures the total tidal force exerted on a grid-cell normalized by its self-gravity. The ellipsoid of the local tidal field is then used to compute the eigenvalues  $t_1$ ,  $t_2$ , and  $t_3$  ( $t_1 \geq t_2 \geq t_3$ ) of the halo tidal tensor. We use  $t_1$  to describe the strength of the halo tidal field at any given grid-cell of  $1 (h^{-1} \text{ Mpc})^3$ .

Fig. 1 shows that grid-cells with higher  $t_1$  have higher mean pressure at a given density in the Illustris simulation, and the result for the EAGLE simulation is qualitatively the same. Apparently, the formation of large scale structure and/or intense feedback in regions of strong tidal field can heat the IGM on large scales.

## 3 METHODS

### 3.1 The matched filter technique

Extracting the tSZE signals reliably requires to optimize the signal-to-noise, since the signal is generally more than an order of magnitude lower than other sources, such as the primary CMB anisotropy, Galactic foreground, and cosmic infrared background. Thus, using a simple aperture photometry can lead to large uncertainties in the results (see e.g. Melin et al. 2006). Here, we employ the matched filter (MF) technique (Haehnelt & Tegmark 1996; Herranz et al. 2002; Melin et al. 2005, 2006), which is designed to minimize source confusions and contamination, and to maximize the signal-to-noise by imposing prior knowledge of the signals and the noise power spectra. In the MF technique, the Fourier transform of the filter that optimizes the signal-to-noise is given by

$$\hat{F}(\mathbf{k}) = \left[ \int \frac{|\hat{\tau}(\mathbf{k}') \hat{B}(\mathbf{k}')|^2}{P(k')} \frac{d^2 k'}{(2\pi)^2} \right]^{-1} \frac{\hat{\tau}(\mathbf{k}) \hat{B}(\mathbf{k})}{P(k)} \quad (3)$$

where, in our application,  $\hat{\tau}(\mathbf{k})$  is the Fourier transform of the projected electron pressure,  $\hat{B}(\mathbf{k})$  is the Fourier transform of the Gaussian beam function that mimics the convolution in the *Planck* observation with the FWHM of  $5'$ , and  $P(k)$  is the noise power spectra. Because the MILCA  $y$ -map is already cleaned of the primary CMB anisotropy,  $P(k) = P_{\text{noise}}$  where  $P_{\text{noise}}$  is the power spectrum of the noise map for the MILCA  $y$ -map, as provided in the *Planck* data release. Both the shape and amplitude of the projected electron pressure profile,  $\hat{\tau}(\mathbf{k})$ , are simultaneously constrained by matching the filters to all pixels, as to be described in details below.

**Table 1.** The constrained parameters for the power-law relation.

Samples	$A^a$	$\rho_{m,0} / \bar{\rho}_m$	$\alpha_1$	$\alpha_2$
all cells	$20 \pm 6.9$	$3.0 \pm 1.5$	$1.7 \pm 0.28$	$2.2 \pm 0.12$
high $t_1$	$25 \pm 26$	$1.1 \pm 2.1$	$1.9 \pm 0.48$	$1.8 \pm 0.26$
mid $t_1$	$21 \pm 20$	$2.1 \pm 3.1$	$1.7 \pm 0.54$	$1.9 \pm 0.20$
low $t_1$	$2.5 \pm 17$	$1.4 \pm 2.5$	$1.8 \pm 0.43$	$2.2 \pm 0.24$

**Notes.**

$a$  The values are in the unit of  $10^{-20} \text{ kg m}^{-1} \text{ s}^{-2}$ .

### 3.2 The pressure - density relation

We assign a value of electron pressure to each of the grid-cells by assuming a simple double power-law relation between the reconstructed matter density field and the pressure:

$$P_e = \begin{cases} A \times (\rho_m / \rho_{m,0})^{\alpha_1}, & \text{if } \rho_m \leq \rho_{m,0} \\ A \times (\rho_m / \rho_{m,0})^{\alpha_2}, & \text{if } \rho_m > \rho_{m,0}. \end{cases} \quad (4)$$

The pressure field is smoothed with a Gaussian kernel of radius  $1 h^{-1} \text{ Mpc}$ , and is integrated along each line of sight to obtain the predicted  $y$ -parameters for all the pixels in in the *Planck*  $y$ -map. The predicted  $y$ -parameter profile at each pixel is used in equation (3) to obtain the corresponding filter, and the filters for all the pixels are matched to the *Planck* map. Finally, we perform the Monte Carlo Markov Chain (MCMC) to constrain the parameters of the double power-law relation so as to yield the best overall match between the filters and the observed  $y$ -map, based on the sum of the  $\chi^2$  over all the pixels. We assume a constant background contribution from free electrons outside the volume in which the density reconstruction was made, and the background level is treated as a free parameter to be constrained with the MCMC. This is expected to be valid as long as the structures lying beyond the boundary of the reconstruction volume are not correlated with the structures within the volume. In this case, the fluctuations of the background do not lead to bias, but increase noise.

## 4 RESULTS

### 4.1 The pressure - density relation

Fig. 3 shows the pressure - density relation obtained from the data, with the constrained parameters listed in Table 1. The orange band shows the  $1\sigma$  scatter based on the uncertainties of the constrained parameters given by the MCMC, representing the dispersion in the relation. The slope of the relation for low-density region is very close to that expected from an adiabatic equation of state,  $P_e \sim \rho^{5/3}$ , but the relation is slightly steeper for dense regions. This indicates that gas in the dense regions may be heated by additional sources, such as supernova and AGN feedback from galaxies residing in these regions, and shocks associated with the formation of large scale structure. As a null test, we randomly shuffle the grid-cells and apply the same method to constrain the rela-

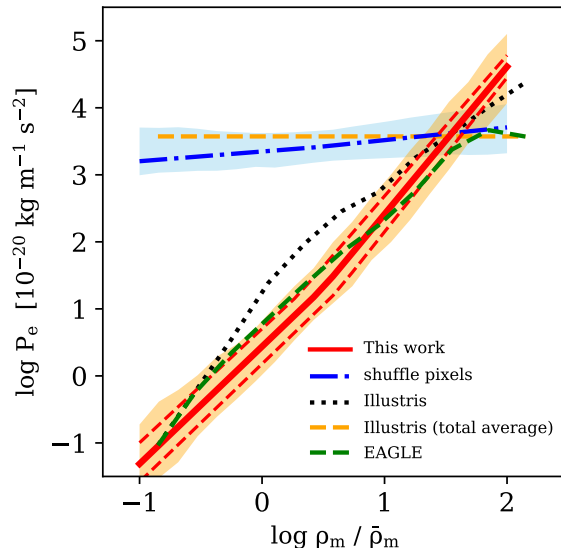


**Figure 3.** The pressure - density relation, compared with the simulations. The red line shows the mean relation obtained with our method, with the orange band showing the  $1\sigma$  dispersion estimated from the uncertainties in the constrained parameters, as given by the MCMC sample. The red dashed lines are the relations constrained separately for the two nearly equal-sized sub-samples of the grid-cells according to the sky region, one including the Sloan Great Wall (Gott et al. 2005), and the other not. The black and green lines show the mean relations from Illustris and EAGLE, respectively. Also, the mean relation obtained from shuffling the grid-cells (dot-dashed), with the band showing the relations from 50 realizations, is compared with that obtained from Illustris (orange dashed).

tion. The mean relation, plotted as the thick blue line, and the relations from a total of 50 realizations, plotted as the sky-blue band, are all flat, as expected from random fluctuations. This demonstrates that our method is able to detect the true relation between the gas and dark matter distribution. Note that the scatter in the constrained pressure - density relation is similar to that among the random samples, indicating that the uncertainty in the constrained relation is dominated by fluctuations of the background/foreground. Finally, we divide the grid-cells into two nearly equal-sized sub-samples according to the sky region they belong to, one including the Sloan Great Wall (Gott et al. 2005) and the other not, and constrain the relation separately for the two sub-samples. The mean relations obtained for the two sub-samples, shown by the red dashed lines, are within the  $1\sigma$  scatter band obtained for the entire sample, indicating that cosmic variance does not affect our results significantly.

We find that using a different smoothing scale, e.g.  $2 h^{-1} \text{ Mpc}$ , leads to no significant change in our results. Choosing an even larger smoothing scale leads to bigger uncertainties in the constrained relations, because of the decreased number of grid-cells. Note that the uncertainty in the reconstructed peculiar velocities is about  $100 \text{ km s}^{-1}$  (see W16), which corresponds to  $\sim 1 h^{-1} \text{ Mpc}$  in real-space positions. Thus, choosing a smoothing scale smaller than  $\sim 1 h^{-1} \text{ Mpc}$  may not be appropriate.

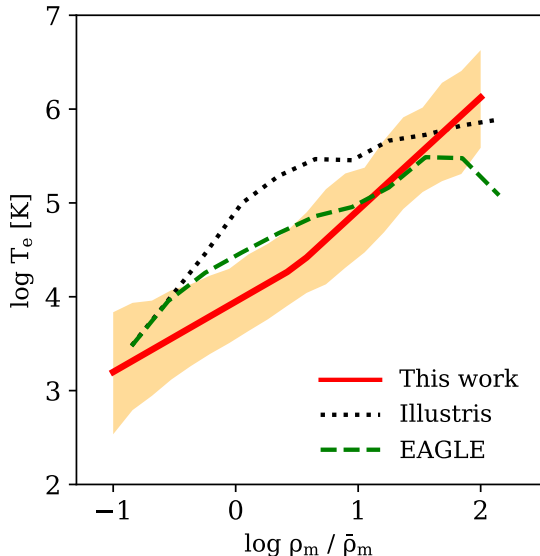


**Figure 4.** The temperature - density relation derived assuming  $\rho_{\text{B,ion}}/\rho_{\text{m}} \sim \Omega_{\text{B}}/\Omega_{\text{m}} = 0.16$  and  $n_{\text{e}} = \rho_{\text{B,ion}} \cdot [(1 + f_{\text{H}})/2m_{\text{p}}]$ , where  $\rho_{\text{B,ion}}$  is the ionized gas density,  $f_{\text{H}} = 0.76$  is the hydrogen mass fraction and  $m_{\text{p}}$  is the proton mass. The red line shows the mean relation obtained with our method, with the orange band showing the  $1\sigma$  dispersion estimated from the uncertainties in the constrained parameters. The dotted and dashed lines show the mean relations from Illustris and EAGLE, respectively.

## 4.2 The temperature - density relation

Assuming that the ionized gas mass fraction with respect to the total mass within the grid-cells approximately equals the cosmic mean baryon fraction, as is motivated by the simulation results shown in Fig. 2, one can convert the observed pressure - density relation to a relation between gas temperature and mass density. Specifically, we assume  $\rho_{\text{B,ion}}/\rho_{\text{m}} \sim \Omega_{\text{B}}/\Omega_{\text{m}} = 0.16$  and  $n_{\text{e}} = \rho_{\text{B,ion}} \cdot [(1 + f_{\text{H}})/2m_{\text{p}}]$ , where  $\rho_{\text{B,ion}}$  is the ionized gas density,  $f_{\text{H}} = 0.76$  is the hydrogen mass fraction and  $m_{\text{p}}$  is the proton mass, to obtain the electron temperature. The mean temperature - density relation thus derived for the entire observational sample is shown in Fig. 4 by the solid line, along with the  $1\sigma$  dispersion estimated from the uncertainties in the constrained parameters. As one can see, the average temperature is about  $10^4$  K in regions of mean density,  $\rho_{\text{m}} \sim \bar{\rho}_{\text{m}}$ , increasing to  $\sim 10^5$  K for  $\rho_{\text{m}} \sim 10\bar{\rho}_{\text{m}}$ , the typical density for cosmic filaments and sheets (e.g. Shen et al. 2006), and to  $> 10^6$  K for  $\rho_{\text{m}} \sim 100\bar{\rho}_{\text{m}}$ , the typical density of dark matter halos.

## 4.3 Dependence on local tidal field

To examine how the pressure - density relation depends on large-scale environment, we divide the grid-cells into three sub-samples, each containing a third of the total number of cells at the density in question, according to the ranking in the halo tidal field strength,  $t_1$ . We then constrain the pressure - density relations for the three sub-samples jointly, assuming different sets of the parameters for each of the sub-samples (see Table 1 for the parameters). The

results are shown in Fig. 5, with the pressure - density relation for each sample normalized by the mean relation shown in Fig. 3. It is clear that, for a given density, the electron pressure is higher in regions of stronger tidal field, but the shapes of the relations are not very different among the sub-samples. This result is consistent with that obtained from gas simulations, as we will see in §4.4. The two breaking points in the relations obtained from the data arise because the relations for the sub-samples have different values of  $\rho_{\text{m},0}$  from that for the total sample.

As mentioned in §2.4, we have tested a number of environmental quantities other than the tidal field as the second parameter that affects the thermal contents of the IGM. Among them, the distance of a grid-cell to the nearest massive halo is found to be nearly as a good indicator as the tidal field both from the simulation and from the application of our method to the observation. This is not surprising, as the local tidal field is strongly correlated with the presence of massive structures nearby.

## 4.4 Comparisons with simulations

In this subsection, we make comparisons of our results with gas simulations. Fig. 3 shows that the pressure - density relation obtained from the data roughly matches those given by the simulations. The result obtained from shuffling the grid-cells is also found to be very similar to the total average pressure from the simulations, as indicated by the horizontal dashed line in Fig. 3. In more detail, the observed pressure - density relation matches well with that given by EAGLE in both amplitude and shape, but Illustris significantly over-predicts the gas pressure in the intermediate density range from  $\sim \bar{\rho}_{\text{m}}$  to  $\sim 10\bar{\rho}_{\text{m}}$ . As mentioned earlier, the difference between Illustris and EAGLE is likely caused by the different implementations of feedback processes adopted in the two simulations. Indeed, as shown in Vogelsberger et al. (2014), the strong AGN feedback adopted in Illustris can heat a significant fraction of the IGM at large distances from over-dense regions, which may explain the high pressure seen in the intermediate density range. Our results, however, suggest that such strong feedback may not be favored by the data.

The dotted and dashed lines in Fig. 4 are the average temperatures obtained directly from Illustris and EAGLE, respectively. Thus, if the ionized baryon fraction is approximately equal to the universal baryon fraction on scales of  $\sim 1 h^{-1}\text{Mpc}$  in the real universe, as is assumed in deriving the temperature - density relation from the data, then the average IGM temperature predicted by Illustris in the density range  $(1 - 10)\bar{\rho}_{\text{m}}$  is too high. The prediction of EAGLE is consistent with the observation, given the uncertainty in the data. This again shows that the data are already capable of providing interesting constraints on models of galaxy formation.

Finally, in Fig. 5, we compare observation and simulation results in their dependence on the strength of local tidal field. Here the simulation results are normalized by the corresponding mean relations shown in Fig. 3. The simulation results are consistent with the observational data in that the gas pressure at a given mass density is higher in regions of stronger tidal field. We have checked that the average ionized gas fraction is quite independent of the tidal

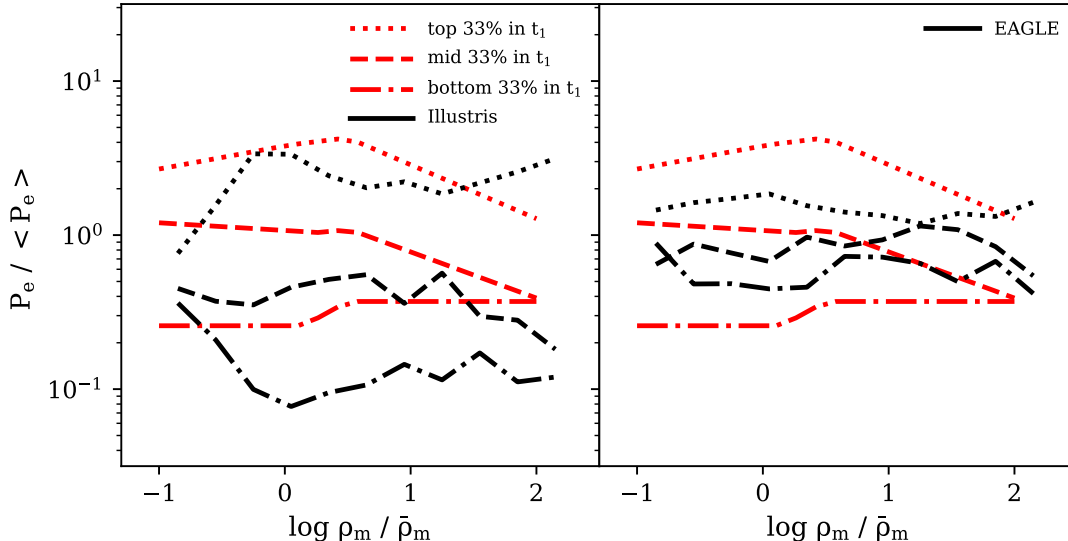


**Figure 5.** The pressure - density relations obtained for the three sub-samples of the grid-cells according to their ranking in the tidal field strength,  $t_1$ , at given density. The red lines in both panels show the mean relations obtained from the data, which are compared with the results of Illustris in the left panel and that of EAGLE in the right panel. For each case, the results are normalized by the corresponding mean relation shown in Fig. 3.

strength in the simulations, and so the higher pressure in stronger tidal field is due to higher gas temperature rather than higher gas density. The dependence on the tidal field predicted by Illustris is much stronger than that by EAGLE. If shock heating by gravitational collapse has similar effects in both simulations, the difference in the tidal field dependence should then be a result of the different prescriptions of feedback used in the two simulations. The feedback effects on the IGM are expected to depend strongly on the local tidal field. For example, a cell with relatively low density but high  $t_1$  must have some massive structures nearby to produce the strong tidal field. Such massive structures are also where strong stellar/AGN feedback is produced. In fact, as can be seen from figure 4 in Vogelsberger et al. (2014), feedback effects on the IGM are clearly more important in the neighborhoods of more massive structures, where the tidal field is also stronger. It is interesting to note that, in both simulations, the strongest tidal field dependence occurs in regions with  $\rho_m \sim \bar{\rho}_m$ , although the signal is rather weak, indicating that the gas temperatures in such regions may be affected the most by feedback from nearby structures. The tidal field dependence obtained from the data is weaker than that predicted by Illustris but stronger than that by EAGLE. We have estimated the velocity dispersion of dark matter particles,  $\sigma$ , in individual grid cells in the simulations, and examined the average of  $\sigma^2$  for cells of different  $\rho_m$  in regions of different tidal strengths. We found that the dependence of  $\sigma^2$  on the tidal strength in the intermediate density range,  $\rho_m \sim (1-10)\bar{\rho}_m$ , is weaker than that of gas temperature, both in the observation and particularly in Illustris. If we take  $\sigma^2$  as a measure of heating by gravitational collapse, then non-gravitational processes, such as stellar and AGN feedback, must have played an important role in heating the IGM in the intermediate density range.

## 5 SUMMARY AND DISCUSSION

In this paper we examine the thermal energy contents of the IGM over three orders of magnitude in both mass density and gas temperature using thermal Sunyaev-Zel'dovich effect (tSZE). Our results are based on *Planck* tSZE map and the cosmic density field, reconstructed for the SDSS DR7 volume and sampled on a grid of cubic cells of  $(1h^{-1}\text{Mpc})^3$ , together with a matched filter technique employed to maximize the signal-to-noise.

Our results obtained by matching all the grid cells show that the pressure - density relation of the IGM is roughly a power law given by an adiabatic equation of state, with some indication of a steepening at densities higher than about 10 times the mean density of the universe. The result from shuffling the grid-cells shows a nearly zero slope for the pressure-density relation, demonstrating that the relation obtained by our method indeed captures the thermal properties of the gas that produces the observed tSZE.

Using the simulation result that the ionized gas mass fractions within individual grid cells are about equal to the universal baryon fraction, we convert the pressure - density relation to a temperature - density relation. The result shows that the average temperature is about  $10^4$  K in regions of mean density,  $\rho_m \sim \bar{\rho}_m$ , increasing to about  $10^5$  K for  $\rho_m \sim 10\bar{\rho}_m$ , the typical density for cosmic filaments and sheets, and to  $> 10^6$  K for  $\rho_m \sim 100\bar{\rho}_m$ , the typical density of virialized dark matter halos.

The thermal energy content of the IGM is also found to be higher in regions of stronger tidal fields. By dividing grid cells into three equal-sized sub-samples according to the local tidal field strength, we find that the average gas temperature in the sub-sample of highest tidal field is a factor of 10 higher than that in the lowest tidal field sub-sample. Such an increase of temperature in intermediate density re-

gions is stronger by a factor of two than that expected from the increase of average velocity dispersion of dark matter in simulations, suggesting that feedback from galaxy formation may be responsible for the increase in gas temperature.

We compare our results with those obtained from two hydrodynamic simulations, Illustris and EAGLE. While the simulations can reproduce the general trends observed in the observation, such as the increases of gas pressure and temperature with dark matter density and the strength of local tidal field, there are significant discrepancies between the two simulations, as well as between the simulations and our observational results. Within the uncertainties of the data, the predictions of EAGLE are consistent with the data. However, Illustris predicts significantly higher gas pressure and temperature in the intermediate density range,  $\rho_m \sim (1 - 10)\bar{\rho}_m$ , than both the observation and EAGLE. The dependence on tidal field strength predicted by Illustris is also too strong in comparison with the observational data and EAGLE. We suspect that these differences are produced by the strong AGN feedback adopted in Illustris that can heat the IGM at large distances from massive structures.

Our results clearly demonstrate the promise of using SZE, combined with reconstructed density field, to study both the IGM and the galaxy formation processes that produce them. This approach is complementary to absorption line studies, in that it is not constrained by a limited number of lines of sight, and that corrections for metallicity and ionization effects are not needed to obtain the total gas mass. It also complements X-ray observations, in that it is more sensitive to the diffuse warm-hot gas that is expected to dominate the IGM. In the future, when high-resolution SZE data are available, the same approach as developed here can be used to study not only the detailed distribution and state of the IGM, but also to investigate how the IGM is related to and affected by galaxies and AGNs in the cosmic web.

## ACKNOWLEDGEMENTS

HJM acknowledges the support from NSF AST-1517528. This work is also supported by the China 973 Program (No. 2015CB857002) and the National Science Foundation of China (grant Nos. 11233005, 11621303, 11522324, 11421303, 11503065, 11673015, 11733004). We thank the Planck collaboration for making the full-sky maps public, and the Virgo Consortium for making the EAGLE simulation data available. The EAGLE simulations were performed using the DiRAC-2 facility at Durham, managed by the ICC, and the PRACE facility Curie based in France at TGCC, CEA, Bruyères-le-Châtel.

## REFERENCES

- Abazajian K. N. et al., 2009, *ApJS*, 182, 543  
Aguirre A., Hernquist L., Schaye J., Katz N., Weinberg D. H., Gardner J., 2001, *ApJ*, 561, 521  
Cen R., Ostriker J. P., 1999, *ApJ*, 514, 1  
Crain R. A. et al., 2015, *MNRAS*, 450, 1937  
Danforth C. W., Shull J. M., 2008, *ApJ*, 679, 194  
Davé R., Hernquist L., Katz N., Weinberg D. H., 1999, *ApJ*, 511, 521  
Davé R. et al., 2001, *ApJ*, 552, 473  
de Graaff A., Cai Y.-C., Heymans C., Peacock J. A., 2017, arXiv:1709.10378  
Ettori S., Baldi A., Balestra I., Gastaldello F., Molendi S., Tozzi P., 2015, *A&A*, 578, A46  
Fukugita M., Hogan C. J., Peebles P. J. E., 1998, *ApJ*, 503, 518  
Fukugita M., Peebles P. J. E., 2004, *ApJ*, 616, 643  
Furlanetto S. R., Loeb A., 2004, *ApJ*, 611, 642  
Gott III J. R. et al., 2005, *ApJ*, 624, 463  
Greco J. P., Hill J. C., Spergel D. N., Battaglia N., 2015, *ApJ*, 808, 151  
Haehnelt M. G., Tegmark M., 1996, *MNRAS*, 279, 545  
Herranz D. et al., 2002, *MNRAS*, 336, 1057  
Hill J. C., Spergel D. N., 2014, *JCAP*, 2, 030  
Hinshaw G. et al., 2013, *ApJS*, 208, 19  
Hojjati A., McCarthy I. G., Harnois-Deraps J., Ma Y.-Z., Van Waerbeke L., Hinshaw G., Le Brun A. M. C., 2015, *JCAP*, 10, 047  
Hurier G., Macías-Pérez J. F., Hildebrandt S., 2013, *A&A*, 558, 118  
Kang X., Jing Y. P., Mo H. J., Börner G., 2005, *ApJ*, 631, 21  
Lim S. H., Mo H. J., Lu Y., Wang H., Yang X., 2017, *MNRAS*, 470, 2982  
Lim S. H., Mo H. J., Li R., Liu Y., Ma Y.-Z., Wang H., Yang X., 2018a, *ApJ*, 854, 181  
Lim S. H., Mo H. J., Wang H., Yang X., 2018b, arXiv:1712.08619  
Ma Y.-Z., Van Waerbeke L., Hinshaw G., Hojjati A., Scott D., Zuntz J., 2015, *JCAP*, 9, 046  
Mantz A. B., Allen S. W., Morris R. G., Simionescu A., Urban O., Werner N., Zhuravleva I., 2017, *MNRAS*, 472, 2877  
McAlpine S. et al., 2016, *Astronomy and Computing*, 15, 72  
McDonald M. et al., 2016, *ApJ*, 826, 124  
Melin J.-B., Bartlett J. G., Delabrouille J., 2005, *A&A*, 429, 417  
Melin J.-B., Bartlett J. G., Delabrouille J., 2006, *A&A*, 459, 341  
Nath B. B., Silk J., 2001, *MNRAS*, 327, 5  
Nelson D., Genel S., Vogelsberger M., Springel V., Sijacki D., Torrey P., Hernquist L., 2015, *MNRAS* 448, 59  
Olive K. A., Steigman G., Walker T. P., 2000, *Physics Reports*, 333, 389  
Planck Collaboration I., 2011, *A&A*, 536, 1  
Planck Collaboration XI., 2013, *A&A*, 557, 52  
Planck Collaboration XIII., 2016, *A&A*, 594, 13  
Planck Collaboration XXII., 2016, *A&A*, 594, 11  
Rasera Y., Teyssier R., 2006, *A&A*, 445, 1  
Remazeilles M. et al., 2011, *MNRAS*, 418, 467  
Schaye J. et al., 2015, *MNRAS* 446, 521  
Shen J., Abel T., Mo H. J., Sheth R. K., 2006, *ApJ*, 645, 783  
Sunyaev R. A., Zeldovich Y. B., 1972, *Comments on Astrophysics and Space Physics*, 4, 173  
Tanimura H., Hinshaw G., McCarthy I. G., Van Waerbeke L., Ma Y.-Z., Mead A., Hojjati A., Tröster T., 2017, arXiv:1709.05024  
Tauber J. A. et al., 2010, *A&A*, 520, 1  
van den Bosch F. C., Yang X., Mo H. J., 2003, *MNRAS*,

- 340, 771
- Van Waerbeke L., Hinshaw G., Murray N., 2014, *Physical Review D*, 89, 023508
- Vogelsberger M. et al., 2014, *MNRAS*, 444, 1518
- Wang H., Mo H. J., Jing Y. P., Guo Y., van den Bosch F. C., Yang X., 2009, *MNRAS*, 394, 398
- Wang H., Mo H. J., Jing Y. P., Yang X., Wang Y., 2011, *MNRAS*, 413, 1973
- Wang H., Mo H. J., Yang X., Zhang Y., Shi J., Jing Y. P., Liu, C., Li S., Kang X., Gao Y., 2016, *ApJ*, 831, 164
- Werner N., Urban O., Simionescu A., Allen S. W., 2013, *Nature*, 502, 656
- Yang X., Mo H. J., van den Bosch F. C., 2003, *MNRAS*, 339, 1057
- Yang X., Mo H. J., van den Bosch F. C., Jing Y. P., 2005, *MNRAS*, 356, 1293
- Yang X., Mo H. J., van den Bosch F. C., Pasquali A., Li C., Barden M., 2007, *ApJ*, 671, 153